Deciphering the Thermal and Electrochemical Behaviors of Dual Redox-Active Iron Croconate Violet Coordination Complexes

Morgane Denis, Jean-Marc Grenèche, Nicolas Gautier, Philippe Poizot, Thomas Devic

Deciphering the thermal and electrochemical behaviors of dual redox-active iron croconate violet coordination complexes

Morgane Denis,[1] Jean-Marc Grenèche,[2] Nicolas Gautier,[1] Philippe Poizot,[1] Thomas Devic[1*]

[1] Nantes Université, CNRS, Institut des Matériaux de Nantes Jean Rouxel, IMN, F-44000 Nantes, France

[2] Institut des Molécules et Matériaux du Mans, IMMM UMR CNRS 6283, Le Mans Université, Le Mans Cedex 9 F-72085, France

ABSTRACT: Interest in coordination compounds based on non-innocent ligands (NILs) for electrochemical energy storage have raised in the last years. We have focused our attention on an overlooked redox active linker, croconate violet, which has not yet been addressed in this field although closely related to standard NILs such as catecholate and tetracyanoquinodimethane (TCNQ). Two anionic complexes consisting of Fe(II) and croconate violet (-2) with balancing potassium cations were isolated and structurally characterized. By a combination on *in* and *ex situ* techniques (powder and single crystal X-ray diffraction, infrared and ^{57}Fe Mössbauer spectroscopies), we have shown that their dehydration occurs through complex patterns, whose reversibility depends on the initial crystal structure, but that the structural rearrangements around the iron cations occur without any oxidation. While electrochemical studies performed in solution clearly shows that both the organic and inorganic parts can be reversibly addressed, in the solid state poor charge storage capacities were initially measured, mainly due to the solubilization of the solids in the electrolyte. By optimizing the formulation of the electrode and the composition of the electrolyte, a capacity of > 100 mAh g^{-1} after 10 cycles could be achieved. This suggests that this family of redox active linkers deserve to be investigated for solid state electrochemical energy storage, although it requires to solve the issues related to the solubilization of the derived coordination compounds.

Introduction

Although unable yet to compete with purely inorganic[1–3] or organic[4,5] electrode materials, coordination compounds,[6–9] and notably coordination polymers such as Metal Organic Frameworks (MOFs)[10–16] have been proposed as alternative electrode materials for the electrochemical energy storage. Whereas their use as electrode material often exhibit a conversion-type electrochemical mechanism (with irreversible bond breakage), some solids can react according to a conventional insertion reaction. First examples of this behavior were based solely on inorganic redox activity (*e.g.* Fe(III/II) in terephthalates MIL-53[17] and MIL-68[18]). Nevertheless, the main advantage of coordination compounds is the possibility to exploit their hybrid nature by combining organic and inorganic redox activities, or, in other words, by combining cationic (metal-centered) and anionic (ligand-centered) redox activites, similarly to what can be observed in selected oxides.[19,20] Initial examples were based on electronically isolated organic and inorganic redox centers,[21] but non innocent ligands (NILs)[22] were rapidly found to be particularly appealing.[23] Apart from the multiredox activity of the derived complexes, the electronic delocalization between the ligand and the metallic cation could expand through the whole framework, providing a suitable electron transport pathway, which is rarely found in conventional coordination networks based on innocent ligands,[24] but is of outmost importance for efficient electrochemical energy storage. So far, few families of NILs have been mainly studied, namely phenolates[25] (mostly catecholate[26–31]) and related bisiminobenzene[32–36] and dithiolene,[37,38] as well as tetracyanoquinodimethane (TNCQ).[39–42] As expected, the derived coordination polymers exhibited multiple and complex electrochemical reactions in the solid state involving both organic and inorganic redox centers (with reversible accommodation of both cations and anions) combined sometimes with partial solubilization and/or demixion.[42,43]

We have here revisited a pseudo-oxocarbon ligand closely related to the aforementioned ligands, namely croconate violet (**CV**$^{2-}$, see Scheme 1). Its disodium salt was reported back in the 1970s by Fatiadi,[44] and was found to present at least four accessible oxidation states (as solute) as deduced by cyclic voltammetry in organic solvents, in good consistency with its extended π system.[44–47] For this reason, its interest as both anolyte and posolyte for redox flow batteries has been recently evaluated.[48] The coordination ability of the dianion towards transition metals and lanthanides has also been explored, notably by the group of Fabre[49–51] and de Oliviera and Machado.[52–57] It has been shown that both oxygen and nitrogen atoms can form coordination bonds with metallic cations.

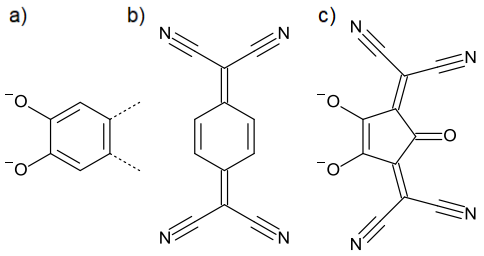

Scheme 1. a) Catecholate (Cat^{2-}), b) tetracyanoquinodimethane (TCNQ); c) croconate violet ($\mathbf{CV}^{2-}$).

We focused our attention on iron, which has several advantages such as high abundancy, low cost and low toxicity when compared to other redox active cations found in standard positive electrode materials (Co, Ni).[58] Two anionic complexes consisting of Fe(II) and croconate violet (-2) with counter balancing alkaline cations (potassium) were isolated and structurally characterized. Such compounds could be considered as interesting candidates for electrochemical energy storage, as they are expected to exhibit reversible electrochemical activities in the solid state centered on both the cation (Fe) and anions (CV). Their dehydration was thoroughly studied by a combination of temperature dependent tools (IR spectroscopy, X-ray powder and single crystal diffraction, electron diffraction, ^{57}Fe Mössbauer spectrometry). Finally, their electrochemical behavior were assessed, first in solution, then in the solid state in Li half-cell, and *ex situ* study by Mössbauer spectrometry was used to shed some light on the redox centered involved.

Results and discussion

1. Synthesis, crystal structures and characterization of the hydrated phases

The synthesis conditions were adapted from those reported by Fabre et al. for the preparation of $K_2Fe(\mathbf{CV})_2(H_2O)_4$ (later labeled $\mathbf{1}(H_2O)_4$).[49] An aqueous solution of the dipotassium salt of $\mathbf{CV}^{2-}$ and iron(II) chloride was evaporated at room temperature in the absence of oxygen (see Supporting Information for details). Note here that higher temperatures (*e.g.* hydrothermal conditions) gave rise to amorphous solids and/or degradation of the **CV** fragment. Complete evaporation over 3 days followed by gentle washing with water to remove KCl led to the expected complex $\mathbf{1}(H_2O)_4$. Upon slowing down the evaporation (completion within 7 to 10 days), another crystalline polymorph (later labelled $\mathbf{2}(H_2O)_2{\cdot}2H_2O$) was isolated. Both compounds are obtained in decent yield (~80%) in pure form, as confirmed by X-ray powder diffraction (XRPD, Figure S4). They both consist of molecular dianionic complexes $Fe(\mathbf{CV})_2^{2-}$ surrounded by potassium ions and water molecules.

The crystal structure of $\mathbf{1}(H_2O)_4$ has already been reported by Fabre et al.[49] The Fe ion presents an octahedral coordination sphere composed of two nitrile groups arising from two **CV** anions, and four water molecules (Figure 1a). The **CV** units further assemble into one-dimensional stacks (shortest intermolecular C···C distances are 3.276(3) and 3.295(3) Å) which could favor extended electron delocalization. This stacking leads to the formation of anionic layers (Figure 1b), which are further separated by potassium ions (Figure 1c). These cations interact with various donor atoms present in the structure, namely nitrogen and oxygen atoms from the ligands, and bound water molecules (see Figure S1 and Table S2 for K-O and K-N distances). The CO, CN and CC bond lengths are similar to those observed in $K_2(\mathbf{CV})\cdot 2H_2O$[59] (see Figure S3), suggesting that the ligand adopts a -2 charge. The Fe-O and Fe-N bond distances (Table S3) support a +2 oxidation state for iron, in line with the chemical formula (K:Fe:CV = 2:1:2). The oxidation state of iron was unambiguously confirmed by ^{57}Fe Mössbauer spectrometry; the value of the isomer shift (1.29 at 77 K) lies in the range expected for a +2 high spin (HS) iron cation (see Table S5).

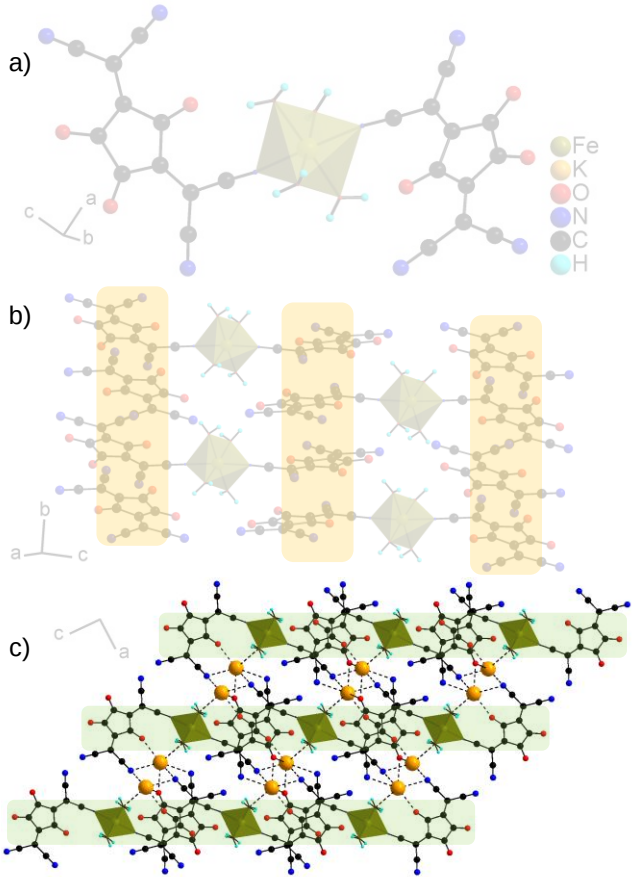

Figure 1. Crystal structure of $K_2Fe(\mathbf{CV})_2(H_2O)_4$ or $\mathbf{1}(H_2O)_4$.[49] a) View of the di-anionic molecular complex; b) stacks of **CV**; c) anionic layers separated by potassium ions.

The structure of $\mathbf{2}(H_2O)_2{\cdot}2H_2O$ was determined by single crystal X-ray diffraction (SCXRD) (see Table S1 for details on data collection and structure refinement). This solid was found to be isostructural with the already reported complexes $K_2M(\mathbf{CV})_2(H_2O)_2{\cdot}2H_2O$ (M = Co, Cu, Mg, Zn[50–52,55]); the structures are essentially the same, with slight variations of M-O distances, as expected. The structure consists again of octahedrally coordinated iron ions bound to two **CV** ligands, but this time each ligand interacts through two neighboring oxygen atoms in a chelating mode. Two water molecules complete the coordination sphere (Figure 2a). These di-anionic flat complexes associate with two potassium ions, where each potassium interacts with two nitrogen and two oxygen atoms arising from both **CV** ligands (see Table S2 for K-O and K-N distances). These three-component molecular entities loosely interact with each other through additional K-N and K-O bonds and N···H-O hydrogen bonds to define layers made of parallel complexes, which are separated by extra water molecules (Figure 2b). Contrary to $\mathbf{1}(H_2O)_4$, no stack of **CV** occurred, but small channels containing water molecules and potassium ions which might favor cationic motion can be identified (Figure 2c).

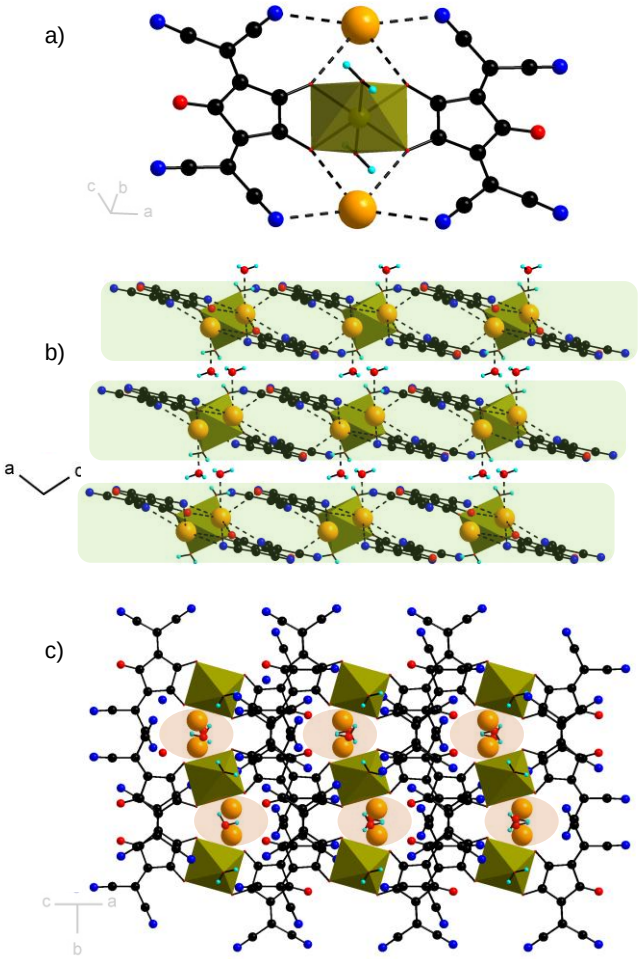

Figure 2. Crystal structure of $K_2Fe(\mathbf{CV})_2(H_2O)_2{\cdot}2H_2O$ or $\mathbf{2}(H_2O)_2{\cdot}2H_2O$. a) View of the di-anionic molecular complex and the surrounding potassium ions; b) layers of complexes separated by water molecules; c) view of the channels containing potassium ions and free water molecules.

Again, the analysis of the CN, CO and CC bond lengths (Figure S3) and the Fe-O bond distances (Table S3) suggests an oxidation state of -2 and +2 for the ligand and the Fe cation respectively. This was confirmed by Mössbauer analysis: a single Fe site was detected, and the value of the isomer shift (1.27 at 77 K) again indicates the presence of +2 high spin Fe cation (see Table S5).

The solids were further characterized by spectroscopic techniques.

Solid state UV-vis reflectance spectra of both $\mathbf{1}(H_2O)_4$, $\mathbf{2}(H_2O)_2{\cdot}2H_2O$ are shown in Figure S8, together with those of $K_2(\mathbf{CV}){\cdot}2H_2O$ for comparison. As expected, a strong absorption feature in the 400-600 nm range, characteristic of the ligand[44] and attributed to several transitions involving the π orbitals centered on the pseudooxocarbon ring as well as on the nitrile moieties[56] is clearly visible in all compounds. Nevertheless, the exact position of absorption bands differs, likely as a consequence of the different coordination modes found in the three solids. In contrast, in diluted aqueous solution (concentration ~ 10^{-5} mol L^{-1}), $\mathbf{1}(H_2O)_4$, $\mathbf{2}(H_2O)_2{\cdot}2H_2O$ and $K_2(\mathbf{CV}){\cdot}2H_2O$ present identical spectra (Figure S9), suggesting the complete dissociation of the complexes under these conditions. When switching to organic solvents found in common battery electrolytes such as propylene carbonate (PC) and tetraethylene glycol dimethyl ether (TEGDME), the spectra are again slightly different, suggesting that the complexes are maintained to some extent after dissolution in these solvents even under extreme dilution (Figure S9).

The solids were further studied by infrared (IR) spectroscopy. Three regions of interest, corresponding the O-H (3700-3200 cm^{-1}), CN (2250-2100 cm^{-1}) and C=O (1750-1550 cm^{-1}) vibrational bands are identified (see Figure S10 for the full spectra). In the high wavenumber region, for $\mathbf{1}(H_2O)_4$, a signal centered at 3320-3200 cm^{-1} is visible, and attributed to the sole type of water molecules found in the crystal structure, *i.e.* water bound to Fe(II). For $\mathbf{2}(H_2O)_2{\cdot}2H_2O$, a signal is found in the same region (3370-3220 cm^{-1}), as well as another one centered at ~ 3600-3480 cm^{-1}. The first one is again attributed to bound water molecules, while the second one is likely associated to the free water molecules identified by XRD analysis. In the intermediate wavenumber region, two bands related to CN vibrations are discernible for all compounds, and likely correspond to in-phase and out-of-phase CN stretching modes.[60] When compared to $K_2(\mathbf{CV}){\cdot}_2H_2O$, these bands are slightly shifted in $\mathbf{2}(H_2O)_2{\cdot}2H_2O$ (2216 and 2199 *vs*. 2222 and 2205 cm^{-1}). For $\mathbf{1}(H_2O)_4$, the shift also occurred (2233 and 2208 cm^{-1}) but is more pronounced for one of the band; the latter has been attributed to the nitrile group bound to Fe(II).[49] Eventually, in the low wavenumber region, bands associated with C=O stretching

modes are seen at 1706 and 1676 cm^{-1} for K_2(**CV**)$\cdot_2H_2O$. [40,55] These bands are almost unchanged in **1**$(H_2O)_4$ (1705 and 1680 cm^{-1}), but become weaker for **2**$(H_2O)_2\cdot 2H_2O$ (1706 and 1682 cm^{-1}). This phenomenon has already been observed in the isostructural compounds made of Co and Cu, and is considered to be a consequence of the formation of carbonyl-cation bonds.[50,51] Below 1640 cm^{-1}, noticeable differences are also detected (Figure S9), but as both water deformation modes and combination of CO and CC vibration modes are expected in this region, a definitive attribution is not straightforward.[49,52,60]

Eventually, the spectroscopic characterizations are in line with the XRD structure analysis. Polymorphs **1**$(H_2O)_4$ and **2**$(H_2O)_2\cdot 2H_2O$, although presenting different complexing modes, could be obtained under very similar experimental conditions. Although the driving force behind this was not identified yet, it suggests that the binding ability of the OCCO motif in **CV** is rather moderate, especially when compared to the parent catecholate ligand. This could be at least partially explained by the complete delocalization of the negative charge on the ligand, and the soft character of the Fe(II) ion.

2. Thermal behavior

We further studied the thermal behavior of both **1**$(H_2O)_4$ and **2**$(H_2O)_2\cdot 2H_2O$, with the aim at investigating the evolution of their structures (oxidation state of the cation, coordination modes) upon water departure. In particular, we wanted to determine whether anhydrous coordination polymers could be generated from these hydrated molecular complexes, which might then be suitable for solid-state electrochemical energy storage due to their potentially reduced solubility. We also wanted to avoid the presence of water as it could give rise to parasitic reactions with the selected electrolytes (containing $LiPF_6$).

The solids were first studied under air, both by thermogravimetry and differential scanning calorimetry (TG-DSC), as well as by temperature dependent XRPD. The corresponding data are shown in Figure 3. For **1**$(H_20)_4$, two major events are identified on the TG-DSC curves: a first endothermic weight loss between 130 and 170°C, and an exothermic one starting at 230°C (Figure 3a). The first one is likely associated with the departure of water molecules while the second one is related to the combustion of the ligand; the experimental weight losses fairly match the theoretical ones considering the formation of Fe_2O_3 and K_2CO_3 (see Table S4). Temperature dependent XRPD indicates that water departure around 130°C is accompanied by a major structural change (Figures 3a and S5), while further weight loss leads to a complete loss of long range order, in line with the degradation of the solid. The reversibility of the transformation was also checked: once heated at 150°C and cooled down to room temperature, the high temperature XRPD pattern remains (Figure S7), indicating that the dehydration is irreversible in our experimental conditions.

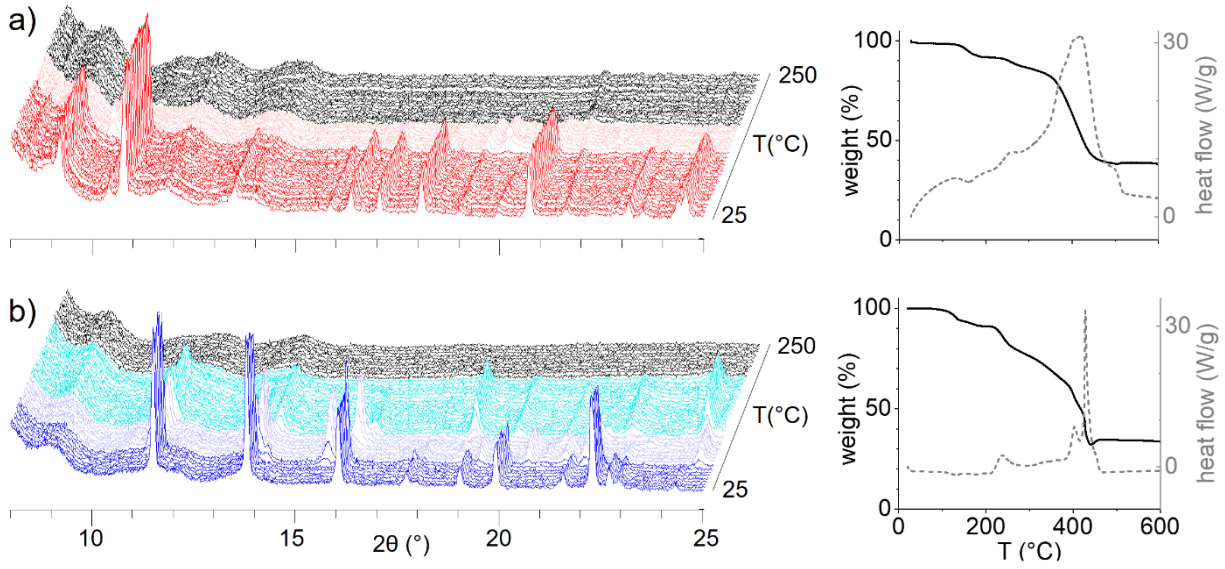

Figure 3. Thermal behavior of a) **1**$(H_2O)_4$ and b) **2**$(H_2O)_2\cdot 2H_2O$. Main figure: temperature dependent XRPD diagram collected every 5°C); inset: TG and DSC curves measured at a heating rate of 5°C min^{-1} under air.

Attempts to solve the structure of the high-temperature phase were carried out. Crystals of **1**$(H_2O)_4$ were heated at 150°C under air, but the water departure is accompanied with their pulverization, which prevents further analysis by SCXRD. Finally, the dehydrated solid was studied by electron diffraction. It was possible to determine the unit cell parameters, but not to solve the complete structure yet (see Supporting Information for details). Spectroscopic techniques were then used to obtain insights on the local structure of the dried solid.

The evolution of the IR spectrum of **1**$(H_2O)_4$ upon heating is shown in Figure 4a. In the range 3700-3200 cm^{-1} corresponding to the O-H stretching modes, a decrease of the intensity of the signal is observed, consistent with the dehydration. Nevertheless, bands remain visible at 200°C, suggesting that the dehydration may not be complete. The changes are more pronounced in the 2250-

2100 cm^{-1} range (CN stretching modes): above 100°C, new bands appear at 2155 and 2135 cm^{-1}, with intensities increasing significantly above 130°C. This is followed by a decrease of the band at 2230 cm^{-1}, which completely vanish above 190°C. On the opposite, the C=O region is almost unaffected. Considering the initial coordination sphere of iron (two nitrile groups and four water molecules), it is expected that upon dehydration, the initially free complexing groups (nitrile and/or carbonyl) would interact with the cation. The IR analysis suggests that only the nitrile groups are involved in this coordination, while the C=O groups remain free Finally, the transformation was followed by ^{57}Fe Mössbauer spectrometry (see Supporting Information for details). The room and high temperature (155°C) spectra are shown in Figure 5a, and the refined values of isomer shift and quadrupolar splitting (IS and QS respectively) are summarized in Table S5. As expected, the water departure is accompanied by a modification of the spectrum, consistent with a strong modification of the environment of iron. The fit of the experimental spectrum is consistent with the presence of two cations with different local environment in a ~1:1 ratio, and the values of IS and QS are in agreement with the presence of exclusively HS Fe(II) cations.

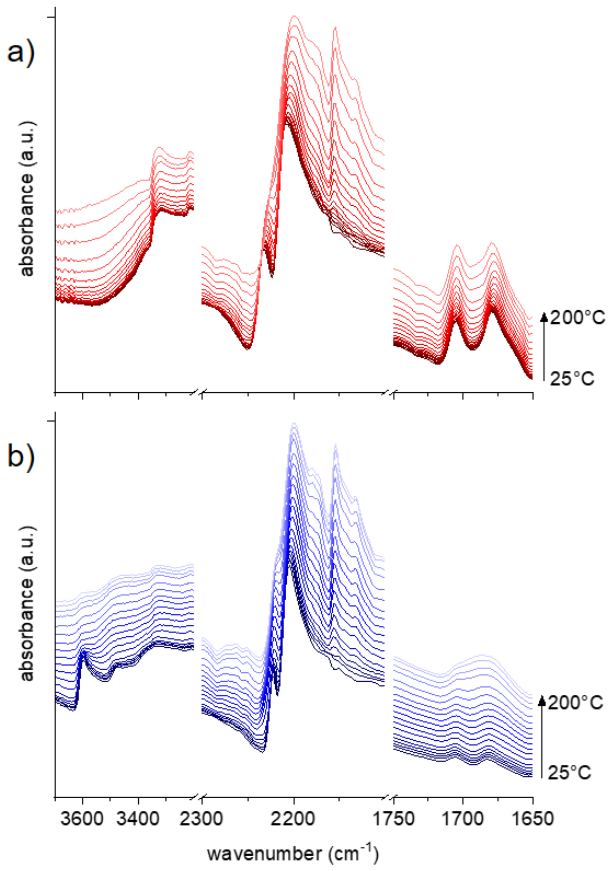

Figure 4. Temperature dependent infrared spectra of a) **1**$(H_2O)_4$ and b) **2**$(H_2O)_2 \cdot 2H_2O$. Data were collected every 10°C from room temperature to 200°C. Areas corresponding to OH, CN and C=O stretching modes are shown.

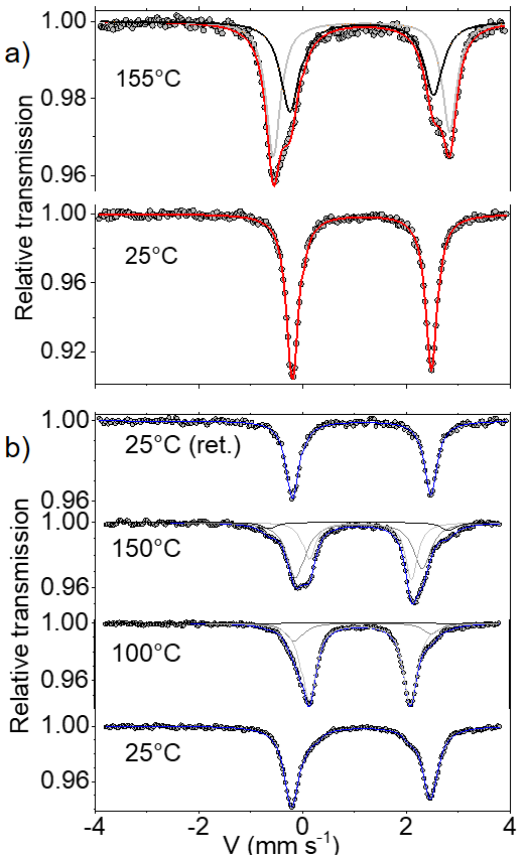

Figure 5. Temperature dependent ^{57}Fe Mössbauer spectra of a) **1**$(H_2O)_4$ and b) **2**$(H_2O)_2{\cdot}2H_2O$. Measurements were carried out at 77 K. The corresponding values of isomer shift and quadrupolar splitting are summarized in Table S5 together with the deduced oxidation state.

The same methodology was applied to **2**$(H_2O)_2{\cdot}2H_2O$. The combustion of the solid (exothermic event) is observed above 220°C (Figure 3b), a value close to those found for **1**(H_2O), and similar to that observed for related catecholate-based complexes (but significantly lower than the ones observed with innocent ligands such as carboxylates). Water departure here occurs in two steps, which are clearly discernible on the TG and DSC curves (endothermic events) in the ranges 105-130 and 130-180°C (Figure 3b). The weight losses are in fair agreement with the successive departure of free (2) and bound (2) water molecules (see Table S4). The departure of the water molecules is accompanied at least two structural changes (Figures 3b and S5), but contrary to **1**$(H_2O)_4$, this transformation is reversible. As shown in Figure S7, once heated up to 170°C and cooled down to room temperature, the initial pattern of the fully hydrated solid **2**$(H_2O)_2{\cdot}2H_2O$ is recovered, although the rehydration path is slightly different from the dehydration one. By gently heating **2**$(H_2O)_2{\cdot}2H_2O$ under air at 120°C, single crystals of the intermediate phase (corresponding to the mallow pattern on Figure 3, see Figure S4) were isolated. Although of moderate quality, it was possible to solve and refine their structure from SCXRD (see Table S1). This solid, formulated **2**$(H_2O)_2$, has a crystal structure closely related to that of the fully hydrated solid (see Figure 2): the same complex is found (Figure 6a), with similar intra-ligand and Fe-O bond distances (Figure S3 and Table S3), indicating that the oxidation states of the ligand and cation are unchanged. The complexes are slightly shifted, so that potassium ions could interact with additional N and O atoms (Figure 6b), especially from ligands belonging to adjacent layers, resulting in additional short interlayer (< 3.5 Å) contacts (Figure S2). Eventually, even in the absence of free water molecules, half of the small channels remains (Figure 6c). Attempts to isolate single crystals of the fully dehydrated solid **2** (*i.e.* without bound water molecules) have not yet been successful, but structural clues were again gained from temperature dependent IR spectroscopy (Figure 4b). In the range corresponding to O-H stretching modes, a strong decrease of the bands at 3600 and 3480 is observed at 90°C, while that at 3320 cm^{-1} occurs at higher temperature. This is in good agreement with the structural results on the hemi-hydrated phase **2**$(H_2O)_2$ and previous attribution of these bands to free and bound water molecules respectively. In the 2250-2100 cm^{-1} range (CN stretching modes), the intensity of the peak at 2220 cm^{-1} decrease, whereas new bands appear at lower wavenumber (2155 and 2133 cm^{-1}). This is accompanied by a strong broadening of the bands at 1706 and 1683 cm^{-1} (C=O stretching modes). All of this suggests that initially free nitrile groups became involved in the coordination of Fe after dehydration, as already found in **1**, but that carbonyl group are also involved, either through a major modification of the initial bonding path (symmetrical chelate, see Figures 2a and 6a), or through the formation of additional Fe-O bonds.

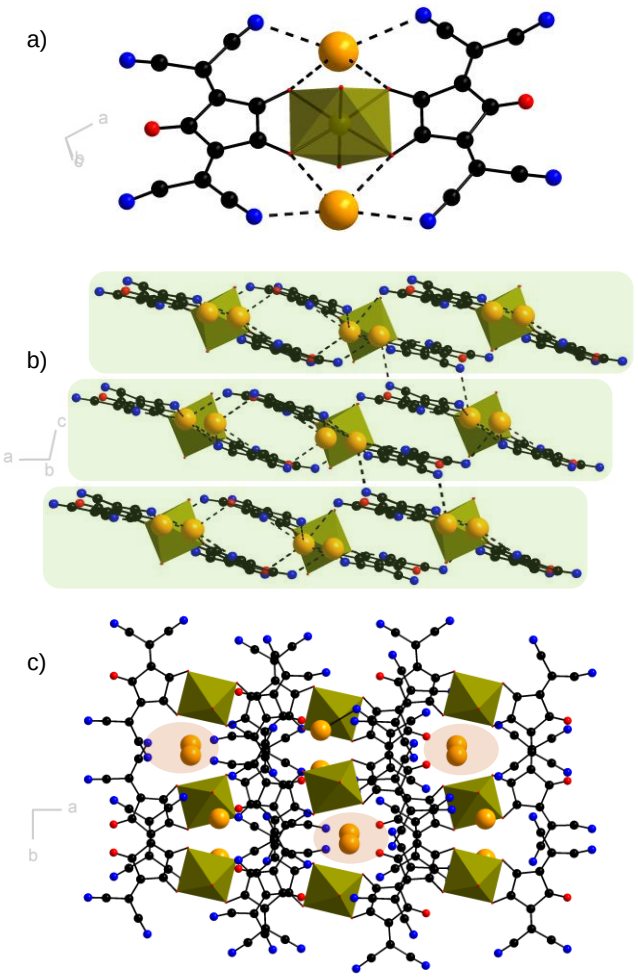

Figure 6. Crystal structure of $K_2Fe(\mathbf{CV})_2(H_2O)$ or $\mathbf{2}(H_2O)_2$. a) View of the di-anionic molecular complex and the surrounding potassium ions; b) layers of complexes; c) view of the channels containing potassium ions.

The evolution of the Mössbauer spectra with temperature reflects the complexity of the thermal behavior identified by diffraction (Figure 5b). Upon heating, at least 3 components, corresponding to different environments of the cation, appear, and their relative amounts vary with temperature (Table S5). Again the derived IS values match with the presence of HS Fe(II) exclusively. When cooled down to room temperature, the initial spectrum is recovered (Figure 5b, top), confirming the reversibility of the dehydration process.

To summarize, considering the whole set of characterizations, it can be concluded that the dehydration of $\mathbf{1}(H_2O)_4$ is irreversible, whereas that of $\mathbf{2}(H_2O)_2{\cdot}2H_2O$ involves the stepwise but reversible departure of free and bound water molecules. In the final state, both compounds contain exclusively Fe(II), surrounded either solely by nitrile groups (**1**) or by both nitrile and carbonyl groups (**2**). Considering the structure of the pristine compounds, such new coordination environments are likely associated with the formation of coordination polymers (rather than molecular complexes). This is *a priori* a beneficial feature for the solid state electrochemical studies since the more numerous and strong the bonds are, the less sensitive these materials will be towards the solvation and dissociation phenomena linked to the polarity of the electrolytes used in batteries.

3. Electrochemical properties

The electrochemical properties of croconate violet dianion salts as solutes have been thoroughly investigated in the past, both in water[44] and organic solvents.[45–48] For example, in acetonitrile, five accessible redox states (charge = -4, -3, -2, -1, 0) were identified by cyclic voltammetry, with related redox potentials at ~-1.7, -1.4, 0.4 and 1.0 V vs. NHE.[48] The fully reduced and fully oxidized forms are rather unstable, while the intermediate radical forms (-3 and -1) were found to be stable at least to some extent, the -1 form being the most stable one. The electrochemical properties of some complexes were also studied by Fabre et al. in solution.[49–51] In DMF, $\mathbf{1}(H_2O)_4$ and the Co and Cu isotypes of $\mathbf{2}(H_2O)_2{\cdot}2H_2O$ were found to present, similarly to **CV**, two oxidations and one reduction steps, all more or less reversible on the time scale of the experiments, with in some cases an extra activity related to the cation (M = Cu, Fe).[49,50] Compared to the free ligand, the shift of the redox potential, was very moderate, but the stability of the complexes in solution was deduced from the comparison of their diffusion coefficients determined by hydrodynamic voltammetry.[49,50] We here first investigated the electrochemical properties of $\mathbf{1}(H_2O)_4$ and $\mathbf{2}(H_2O)_2{\cdot}2H_2O$ by cyclic voltammetry in solution

(concentration ~ 1 mM), using a standard battery electrolyte (1 M $LiClO_4$ in PC) and a lithium foil as the counter electrode. For comparison, K_2**CV**·$2H_2O$ was studied in the same conditions; the corresponding results are shown in Figure 7. As expected, two seemingly reversible oxidation processes are observed for K_2**CV**·$2H_2O$ at 3.5 and 4.0 V vs. Li^+/Li, respectively (Figure 7a). Considering the standard potential of the Li^+/Li redox couple (−3.04 V vs. NHE), these potentials rather match with those reported earlier. In reduction, a poorly reversible process is detected at 2.2 V vs. Li^+/Li, a value slightly higher that expected for the reduction of CV^{2-} to CV^{3-}. The cyclic voltammograms of both complexes are related to the one of pristine croconate violet, but also present additional signals. Both complexes present a seemingly irreversible reduction at 2.3 V, very similar to that found for K_2**CV**·$2H_2O$, suggesting that the reduction is not affected by the complexation. The behavior in oxidation is more complex. A reversible oxidation centered at 3.0 V is detected, while at higher potential, many unresolved events are seen, but their exact position depends on the complex (oxidation at 3.5, 3.9 and 4.2 V vs. Li^+/Li, for **1**$(H_2O)_4$, and 3.3, 3.7 and 3.9 V vs. Li^+/Li for **2**$(H_2O)_2$·$2H_2O$). The fact that all solids present different events suggests that their structures are maintained in solution at least to some extent. The oxidation occurring at 3.0 V is only visible in the complexes and is in the expected range for Fe(III)/Fe(II) redox system; it is then attributed to a metal-centered process. Oxidation occurring at higher potential are thus attributed to ligand-centered processes. The fact that the oxidations of the linker are split in many events suggests that in both complexes, electronic communication occurs between the ligands.

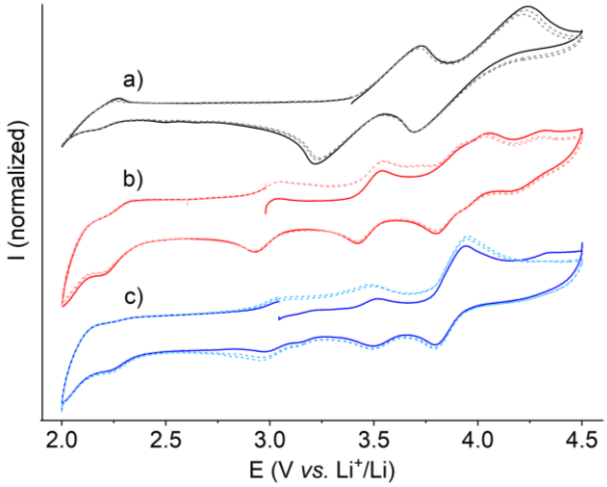

Figure 7. Cyclic voltammograms recorded onto a Pt electrode at a scan rate of 20 mV s^{-1} by starting with an anodic sweep (electrolyte: 1 M $LiClO_4$ in PC). a) K_2**CV**·$2H_2O$, b) **1**$(H_2O)_4$, c) **2**$(H_2O)_2$·$2H_2O$. Plain lines correspond to the first cycle, dashed lines to the second and third cycles.

In order to further assess the electrochemical behavior of the title complexes in the solid state, composite electrodes prepared by grinding with pestle and mortar **1** or **2** with conducting carbon (weight ratio ~2:1) was electrochemically tested in Li half-cells under galvanostatic cycling conditions. The electrolyte consisting in 1 M $LiPF_6$ in a 1 : 1 mixture of ethylene carbonate (EC) and dimethyl carbonate (DMC) was first considered (see Supporting Information for details). Note that such studies were performed on the anhydrous phases to promote polymerization (lower solubility) as well as prevent side-reactions with the electrolyte. In principle, if one accounts from 2 redox processes per ligand (one in oxidation and one in reduction) together with one potential oxidation per iron, a maximal theoretical specific capacity of 221 mAh g^{-1} is expected (scheme 2). Alternatively, this theoretical capacity could be restricted to 177 mAh g^{-1} if the iron center is not electroactive. Note here that the second oxidation of the ligands (from $CV^{\cdot-}$ to CV^0) is not targeted, as it would strongly favor the dissociation of the complexes.

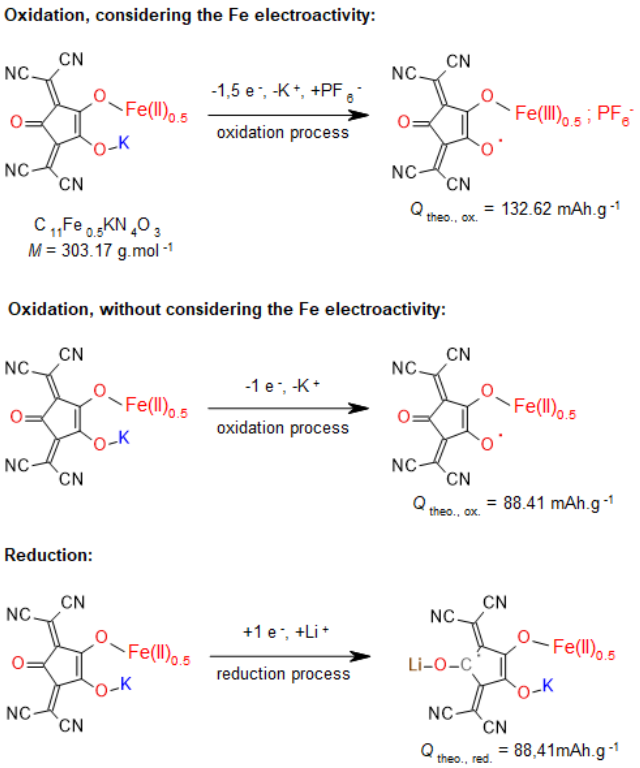

Scheme 2. Possible electrochemical reactions both in oxidation and in reduction, respectively. For the sake of clarity, only half of a complex is shown.

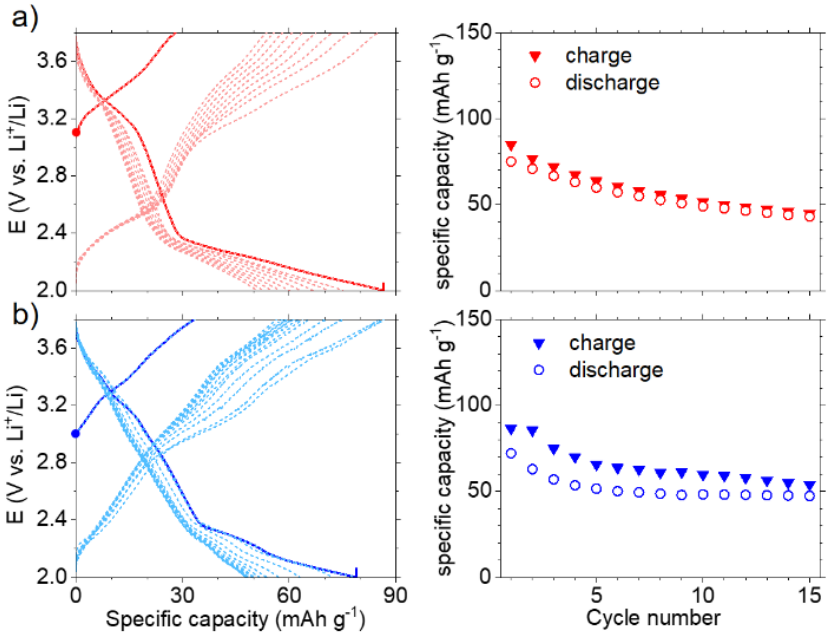

Figure 8. Electrochemical behavior upon galvanostatic cycling of a) **1** and b) **2** electrode materials measured in Li half-cell (electrolyte: 1 M $LiPF_6$ in EC/DMC). Left: potential vs. specific capacity curve (plain lines correspond to the first cycle, dashed lines to the subsequent cycles); right: corresponding capacity retention curves.

Systematically, the galvanostatic cycling was started by a charge process (oxidation) with a potential scan ranging from 2 to 3.8 V vs. Li^+/Li recorded at a cycling rate of 1 e^-/1 Li^+ exchanged per mol of **1** or **2** in 5 h. The corresponding potential vs. specific capacity curves together with the capacity retention are shown in Figure 8.

The electrochemical behavior of both complexes are quite similar. During the first oxidation (charge), one can observe the recorded electrochemical trace is featureless to 3.8 V vs. Li^+/Li. The as-obtained specific capacity value is ~30 mAh g^{-1}, which is quite lower than ~88 mAh g^{-1} for one-electron reaction (scheme 2); the latter being partially recovered during the subsequent reduction (discharge). Below 3 V another electrochemical step occurs characterized by a sharp potential drop followed by a sloppy plateau

at an average potential of 2.1 V vs. Li^+/Li. The overall discharge capacity is of 85 and 79 mAh g^{-1} for **1** and **2,** respectively, in relatively good accordance with the expected value for the one-electron reaction in reduction (scheme 2). Upon cycling, this series of electrochemical steps progressively vanished giving rise to a recovered capacity drop down to 45 and 54 mAh g^{-1} after 15 cycles for **1** and **2,** respectively. Overall, no major difference was detected between **1** and **2**, indicating that their solid state redox behavior is poorly sensitive to the structure, or that strong rearrangements occur in the presence of the electrolyte or upon cycling. Quite importantly, *post-mortem* inspections of the electrochemical cells after cycling suggested that partial solubilization of the material could be at the origin of the poor capacity retention. Further studies were therefore conducted on compound **1** only. We then attempted to improve the performance by playing on the formulation of the electrode and the composition of the electrolyte. First, the large size of the pristine crystallites (typically 50-100 microns before grinding) could prevent the access to all redox centers and then explain the poor initial capacity. To reduce the particle size and improve the contact between the active material and the conducing additive, new electrodes were prepared by freeze-drying process (see Figure S6 and Supporting Information for details). The use of concentrated electrolytes has been shown to decrease the solubility of redox-active coordination polymers and prevent capacity fading.[41] We followed here the same strategy using electrolytes composed of PC and $LiClO_4$ at various concentrations (1, 3.5, 5 and 7 M). The resulting potential *vs.* capacity and capacity retention curves are shown in Figure 9. With highly concentrated electrolytes (5 and 7 M), contrary to previous findings on CuTCNQ,[41] low initial capacities were measured. We tentatively attributed this bad performance to moderate ionic conductivity of the electrolyte at such a scan rate (C/5), and/or to poor wetting of the separator arising from the high viscosity of the electrolyte. For lower electrolyte concentration (1 and 3.5 M), improved initial discharge capacities were obtained (124 and 137 mAh g^{-1}), suggesting that the modification of the formulation of the electrodes was successful. Upon cycling, better capacity retentions were obtained, especially with the 3.5 M electrolyte (-19% after 10 cycles), confirming that the reduction the solubility has a favorable impact on this retention.

While the reduction at low potential could only be related to the ligand (**CV**$^{2-}$ to **CV**$^{3-}$), preliminary *ex situ* experiments Mössbauer were conducted to gain insight into the oxidation process (Figure S11 and Table S6). The spectrum of the electrodes soaked in the electrolyte was measured at rest (~3.0 V vs. Li^+/Li), and after oxidation at 3.8 V vs. Li^+/Li. At 300 K, only Fe(II) is detected in both cases, suggesting that the iron is not oxidized, and hence that the redox activity is exclusively ligand centered. Nevertheless, this experiment was carried out *ex situ* with a delay (~days) between the electrochemical oxidation and the spectroscopic measurement; self-discharge (accompanied with the reduction of Fe(III) to Fe(II)) cannot be completely ruled out. *Operando* Mössbauer measurements will be necessary to clarify this point.

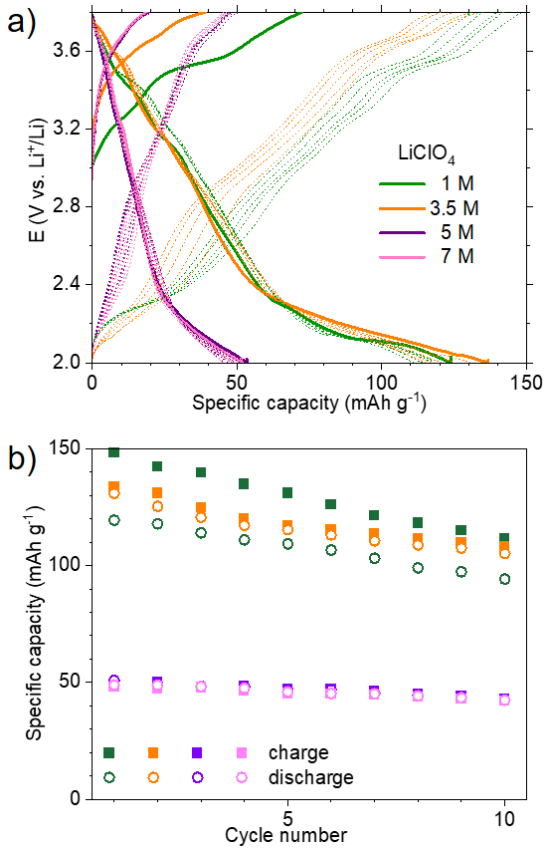

Figure 9. Electrochemical behavior upon galvanostatic cycling of **1** measured in Li half-cell (electrolyte: various concentrations of $LiClO_4$ in PC). a) Potential vs. specific capacity curves (plain lines correspond to the first cycles, dashed lines to the following cycles); b) corresponding capacity retention curves.

Conclusion

We here report two polymorphic complexes based on the redox active Fe(II) center combined with the croconate violet organic unit. These solids, formulated $K_2Fe(\mathbf{CV})_2(H_2O)_4$, present very distinct coordination features although prepared in closely related experimental conditions. We have shown that their dehydration leads to the modification of the coordination environment of iron, but without any oxidation of this cation even in the presence of air. Whereas the electrochemical studies performed in solution clearly showed that both the organic and inorganic parts are electroactive in solution, in the solid state poor charge storage capacities were initially measured, mainly due to the solubilization of the solids in the electrolyte. By optimizing the formulation of the electrode and the composition of the electrolyte, a capacity of > 100 mAh g^{-1} after 10 cycles could be achieved. Although this performance is clearly inferior to that of conventional electrode materials and of MOFs based on NILs mentioned in the introduction, this study suggests that this overlooked family of ligands (CV, but also the related mono- and tris-(dicyanomethylene)croconate)[40,43] deserves to be reinvestigated. However, the solubility issues must be circumvented by an electrolyte management (for instance the use of a solid electrolyte), or by the preparation of more condensed, and probably less soluble, polymeric coordination compounds.

ASSOCIATED CONTENT

Supporting Information. Synthesis procedures, structure determination, detailed characterizations. This material is available free of charge via the Internet at http://pubs.acs.org.

AUTHOR INFORMATION

Corresponding Author

* thomas.devic@cnrs-imn.fr

Author Contributions

MD synthesis and characterizations; JMG: Mössbauer spectrometry; PP: electrochemical studies; NG: electron diffraction, T.D: conception of the work, structure determination. The manuscript was written through contributions of all authors. All authors have given approval to the final version of the manuscript.

ACKNOWLEDGMENT

Funding (fellowship for M.D) from the region Pays de la Loire (project PSR 'MatHySE2') is acknowledged. Funding by the French Contrat Plan État-Région and the European Regional Development Fund of Pays de la Loire, the CIMEN Electron Microscopy Center in Nantes, is gratefully acknowledged. S. Grolleau is thanked for the thermal analyses, and S. Renault for fruitful discussions.

REFERENCES

(1) Masquelier, C.; Croguennec, L. Polyanionic (Phosphates, Silicates, Sulfates) Frameworks as Electrode Materials for Rechargeable Li (or Na) Batteries. *Chem. Rev.* **2013**, *113*, 6552–6591.

(2) Armand, M.; Axmann, P.; Bresser, D.; Copley, M.; Edström, K.; Ekberg, C.; Guyomard, D.; Lestriez, B.; Novák, P.; Petranikova, M.; Porcher, W.; Trabesinger, S.; Wohlfahrt-Mehrens, M.; Zhang, H. Lithium-Ion Batteries – Current State of the Art and Anticipated Developments. *J. Power Sources* **2020**, *479*, 228708. https://doi.org/10.1016/j.jpowsour.2020.228708.

(3) Jin, T.; Li, H.; Zhu, K.; Wang, P.-F.; Liu, P.; Jiao, L. Polyanion-Type Cathode Materials for Sodium-Ion Batteries. *Chem. Soc. Rev.* **2020**, *49* (8), 2342–2377. https://doi.org/10.1039/C9CS00846B.

(4) Poizot, P.; Gaubicher, J.; Renault, S.; Dubois, L.; Liang, Y.; Yao, Y. Opportunities and Challenges for Organic Electrodes in Electrochemical Energy Storage. *Chem. Rev.* **2020**, *120* (14), 6490–6557. https://doi.org/10.1021/acs.chemrev.9b00482.

(5) Schon, T. B.; McAllister, B. T.; Li, P.-F.; Seferos, D. S. The Rise of Organic Electrode Materials for Energy Storage. *Chem. Soc. Rev.* **2016**, *45* (22), 6345–6404. https://doi.org/10.1039/C6CS00173D.

(6) Lakraychi, A. E.; De Kreijger, S.; Gupta, D.; Elias, B.; Vlad, A. Phendione–Transition-Metal Complexes with Bipolar Redox Activity for Lithium Batteries. *ChemSusChem* **2020**, *13* (9), 2225–2231. https://doi.org/10.1002/cssc.201903290.

(7) Sy, A.; Bhatti, A. I.; Hamidouche, F.; Bacq, O. L.; Lecarme, L.; Leprêtre, J.-C. Correlation of Electrochemical and Ab Initio Investigations of Iron Poly-Bipyridine Coordination Complexes for Battery Applications: Impact of the Anionic Environment and the Local Geometries of the Redox Complexes on the Electrochemical Response. *Phys. Chem. Chem. Phys.* **2020**, *22* (41), 24077–24085. https://doi.org/10.1039/D0CP01576H.

(8) Gao, P.; Chen, Z.; Zhao-Karger, Z.; Mueller, J. E.; Jung, C.; Klyatskaya, S.; Diemant, T.; Fuhr, O.; Jacob, T.; Behm, R. J.; Ruben, M.; Fichtner, M. A Porphyrin Complex as a Self-Conditioned Electrode Material for High-Performance Energy Storage. *Angew. Chem. Int. Ed.* **2017**, *56* (35), 10341–10346. https://doi.org/10.1002/anie.201702805.

(9) Zheng, Q.; Niu, Z.; Ye, J.; Zhang, S.; Zhang, L.; Li, L.; Zhao, Y.; Zhang, X. High Voltage, Transition Metal Complex Enables Efficient Electrochemical Energy Storage in a Li-Ion Battery Full Cell. *Adv. Funct. Mater.* **2017**, *27* (4), 1604299. https://doi.org/10.1002/adfm.201604299.

(10) Xu, Y.; Li, Q.; Xue, H.; Pang, H. Metal-Organic Frameworks for Direct Electrochemical Applications. *Coord. Chem. Rev.* **2018**, *376*, 292–318. https://doi.org/10.1016/j.ccr.2018.08.010.

(11) Zhou, J.; Wang, B. Emerging Crystalline Porous Materials as a Multifunctional Platform for Electrochemical Energy Storage. *Chem. Soc. Rev.* **2017**, *46* (22), 6927–6945. https://doi.org/10.1039/C7CS00283A.

(12) Zhang, L.; Liu, H.; Shi, W.; Cheng, P. Synthesis Strategies and Potential Applications of Metal-Organic Frameworks for Electrode Materials for Rechargeable Lithium Ion Batteries. *Coord. Chem. Rev.* **2019**, *388*, 293–309. https://doi.org/10.1016/j.ccr.2019.02.030.

(13) Liu, J.; Xie, D.; Shi, W.; Cheng, P. Coordination Compounds in Lithium Storage and Lithium-Ion Transport. *Chem. Soc. Rev.* **2020**, *49* (6), 1624–1642. https://doi.org/10.1039/C9CS00881K.

(14) Schneemann, A.; Dong, R.; Schwotzer, F.; Zhong, H.; Senkovska, I.; Feng, X.; Kaskel, S. 2D Framework Materials for Energy Applications. *Chem. Sci.* **2021**, *12* (5), 1600–1619. https://doi.org/10.1039/D0SC05889K.

(15) Wang, Z.; Tao, H.; Yue, Y. Metal-Organic-Framework-Based Cathodes for Enhancing the Electrochemical Performances of Batteries: A Review. *ChemElectroChem* **2019**, *6* (21), 5358–5374. https://doi.org/10.1002/celc.201900843.

(16) Devic, T. The Potential of MOFs in the Field of Electrochemical Energy Storage. In *Metal-Organic Frameworks in Biomedical and Environmental Field*; Springer Nature, 2021; pp 111–154.

(17) Férey, G.; Millange, F.; Morcrette, M.; Serre, C.; Doublet, M.-L.; Grenèche, J.-M.; Tarascon, J.-M. Mixed-Valence Li/Fe-Based Metal-Organic Frameworks with Both Reversible Redox and Sorption Properties. *Angew. Chem. Int. Ed.* **2007**, *46*, 3259–3263.

(18) Fateeva, A.; Horcajada, P.; Devic, T.; Serre, C.; Marrot, J.; Grenèche, J.-M.; Morcrette, M.; Tarascon, J.-M.; Maurin, G.; Férey, G. Synthesis, Structure, Characterization, and Redox Properties of the Porous MIL-68(Fe) Solid. *Eur. J. Inorg. Chem.* **2010**, *2010*, 3789–3794.

(19) Saubanère, M.; McCalla, E.; Tarascon, J.-M.; Doublet, M.-L. The Intriguing Question of Anionic Redox in High-Energy Density Cathodes for Li-Ion Batteries. *Energy Environ. Sci.* **2016**, *9* (3), 984–991. https://doi.org/10.1039/C5EE03048J.

(20) Li, M.; Liu, T.; Bi, X.; Chen, Z.; Amine, K.; Zhong, C.; Lu, J. Cationic and Anionic Redox in Lithium-Ion Based Batteries. *Chem. Soc. Rev.* **2020**, *49* (6), 1688–1705. https://doi.org/10.1039/C8CS00426A.

(21) Zhang, Z.; Yoshikawa, H.; Awaga, K. Monitoring the Solid-State Electrochemistry of Cu(2,7-AQDC) (AQDC = Anthraquinone Dicarboxylate) in a Lithium Battery: Coexistence of Metal and Ligand Redox Activities in a Metal-Organic Framework. *J. Am. Chem. Soc.* **2014**, *136*, 16112–16115.

(22) Kaim, W. Manifestations of Noninnocent Ligand Behavior. *Inorg. Chem.* **2011**, *50*, 9752–9765.

(23) Liu, J.; Song, X.; Zhang, T.; Liu, S.; Wen, H.; Chen, L. 2D Conductive Metal–Organic Frameworks: An Emerging Platform for Electrochemical Energy Storage. *Angew. Chem. Int. Ed.* **2021**, *60* (11), 5612–5624. https://doi.org/10.1002/anie.202006102.

(24) Xie, L. S.; Skorupskii, G.; Dincă, M. Electrically Conductive Metal–Organic Frameworks. *Chem. Rev.* **2020**, *120* (16), 8536–8580. https://doi.org/10.1021/acs.chemrev.9b00766.

(25) Aubrey, M. L.; Long, J. R. A Dual-Ion Battery Cathode via Oxidative Insertion of Anions in a Metal-Organic Framework. *J. Am. Chem. Soc.* **2015**, *137*, 13594–13602.

(26) Nam, K. W.; Park, S. S.; dos Reis, R.; Dravid, V. P.; Kim, H.; Mirkin, C. A.; Stoddart, J. F. Conductive 2D Metal-Organic Framework for High-Performance Cathodes in Aqueous Rechargeable Zinc Batteries. *Nat. Commun.* **2019**, *10* (1), 1–10. https://doi.org/10.1038/s41467-019-12857-4.

(27) Kon, K.; Uchida, K.; Fuku, K.; Yamanaka, S.; Wu, B.; Yamazui, D.; Iguchi, H.; Kobayashi, H.; Gambe, Y.; Honma, I.; Takaishi, S. Electron-Conductive Metal–Organic Framework, Fe(Dhbq)(Dhbq = 2,5-Dihydroxy-1,4-Benzoquinone): Coexistence of Microporosity and Solid-State Redox Activity. *ACS Appl. Mater. Interfaces* **2021**, *13* (32), 38188–38193. https://doi.org/10.1021/acsami.1c06571.

(28) Taniguchi, K.; Chen, J.; Sekine, Y.; Miyasaka, H. Magnetic Phase Switching in a Tetraoxolene-Bridged Honeycomb Ferrimagnet Using a Lithium Ion Battery System. *Chem. Mater.* **2017**, *29* (23), 10053–10059. https://doi.org/10.1021/acs.chemmater.7b03691.

(29) Ziebel, M. E.; Ondry, J. C.; Long, J. R. Two-Dimensional, Conductive Niobium and Molybdenum Metal–Organic Frameworks. *Chem. Sci.* **2020**, *11* (26), 6690–6700. https://doi.org/10.1039/D0SC02515A.

(30) Dong, H.; Gao, H.; Geng, J.; Hou, X.; Gao, S.; Wang, S.; Chou, S. Quinone-Based Conducting Three-Dimensional Metal–Organic Framework as a Cathode Material for Lithium-Ion Batteries. *J. Phys. Chem. C* **2021**, *125* (38), 20814–20820. https://doi.org/10.1021/acs.jpcc.1c06870.

(31) Gu, S.; Bai, Z.; Majumder, S.; Huang, B.; Chen, G. Conductive Metal–Organic Framework with Redox Metal Center as Cathode for High Rate Performance Lithium Ion Battery. *J. Power Sources* **2019**, *429*, 22–29. https://doi.org/10.1016/j.jpowsour.2019.04.087.

(32) Wada, K.; Sakaushi, K.; Sasaki, S.; Nishihara, H. Multielectron-Transfer-Based Rechargeable Energy Storage of Two-Dimensional Coordination Frameworks with Non-Innocent Ligands. *Angew. Chem. Int. Ed.* **2018**, *57* (29), 8886–8890. https://doi.org/10.1002/anie.201802521.

(33) Chen, Y.; Tang, M.; Wu, Y.; Su, X.; Li, X.; Xu, S.; Zhuo, S.; Ma, J.; Yuan, D.; Wang, C.; Hu, W. A One-Dimensional π–d Conjugated Coordination Polymer for Sodium Storage with Catalytic Activity in Negishi Coupling. *Angew. Chem. Int. Ed.* **2019**, *58* (41), 14731–14739. https://doi.org/10.1002/anie.201908274.

(34) Wang, L.; Ni, Y.; Hou, X.; Chen, L.; Li, F.; Chen, J. A Two-Dimensional Metal–Organic Polymer Enabled by Robust Nickel–Nitrogen and Hydrogen Bonds for Exceptional Sodium-Ion Storage. *Angew. Chem. Int. Ed.* **2020**, *59* (49), 22126–22131. https://doi.org/10.1002/anie.202008726.

(35) Park, J.; Lee, M.; Feng, D.; Huang, Z.; Hinckley, A. C.; Yakovenko, A.; Zou, X.; Cui, Y.; Bao, Z. Stabilization of Hexaaminobenzene in a 2D Conductive Metal–Organic Framework for High Power Sodium Storage. *J. Am. Chem. Soc.* **2018**, *140* (32), 10315–10323. https://doi.org/10.1021/jacs.8b06020.

(36) Kapaev, R. R.; Olthof, S.; Zhidkov, I. S.; Kurmaev, E. Z.; Stevenson, K. J.; Meerholz, K.; Troshin, P. A. Nickel(II) and Copper(II) Coordination Polymers Derived from 1,2,4,5-Tetraaminobenzene for Lithium-Ion Batteries. *Chem. Mater.* **2019**, *31* (14), 5197–5205. https://doi.org/10.1021/acs.chemmater.9b01366.

(37) Wu, Y.; Chen, Y.; Tang, M.; Zhu, S.; Jiang, C.; Zhuo, S.; Wang, C. A Highly Conductive Conjugated Coordination Polymer for Fast-Charge Sodium-Ion Batteries: Reconsidering Its Structures. *Chem. Commun.* **2019**, *55* (73), 10856–10859. https://doi.org/10.1039/C9CC05679C.

(38) Wu, Z.; Adekoya, D.; Huang, X.; Kiefel, M. J.; Xie, J.; Xu, W.; Zhang, Q.; Zhu, D.; Zhang, S. Highly Conductive Two-Dimensional Metal–Organic Frameworks for Resilient Lithium Storage with Superb Rate Capability. *ACS Nano* **2020**, *14* (9), 12016–12026. https://doi.org/10.1021/acsnano.0c05200.

(39) Fang, C.; Huang, Y.; Yuan, L.; Liu, Y.; Chen, W.; Huang, Y.; Chen, K.; Han, J.; Liu, Q.; Huang, Y. A Metal–Organic Compound as Cathode Material with Superhigh Capacity Achieved by Reversible Cationic and Anionic Redox Chemistry for High-Energy Sodium-Ion Batteries. *Angew. Chem. Int. Ed.* **2017**, *56* (24), 6793–6797. https://doi.org/10.1002/anie.201701213.

(40) Ma, J.; Zhou, E.; Fan, C.; Wu, B.; Li, C.; Lu, Z.-H.; Li, J. Endowing CuTCNQ with a New Role: A High-Capacity Cathode for K-Ion Batteries. *Chem. Commun.* **2018**, *54* (44), 5578–5581. https://doi.org/10.1039/C8CC00802G.

(41) Huang, Y.; Fang, C.; Zhang, W.; Liu, Q.; Huang, Y. Sustainable Cycling Enabled by a High-Concentration Electrolyte for Lithium-Organic Batteries. *Chem. Commun.* **2019**, *55* (5), 608–611. https://doi.org/10.1039/C8CC09307E.

(42) Dühnen, S.; Nölle, R.; Wrogemann, J.; Winter, M.; Placke, T. Reversible Anion Storage in a Metal-Organic Framework for Dual-Ion Battery Systems. *J. Electrochem. Soc.* **2019**, *166* (3), A5474–A5482. https://doi.org/10.1149/2.0681903jes.

(43) Chang, C.-H.; Li, A.-C.; Popovs, I.; Kaveevivitchai, W.; Chen, J.-L.; Chou, K.-C.; Kuo, T.-S.; Chen, T.-H. Elucidating Metal and Ligand Redox Activities of a Copper-Benzoquinoid Coordination Polymer as the Cathode for Lithium-Ion Batteries. *J. Mater. Chem. A* **2019**, *7* (41), 23770–23774. https://doi.org/10.1039/C9TA05244E.

(44) Fatiadi, A. J. Synthesis of 1,3-(Dicyanomethylene)Croconate Salts. New Bond-Delocalized Dianion, "Croconate Violet." *J. Am. Chem. Soc.* **1978**, *100* (8), 2586–2587. https://doi.org/10.1021/ja00476a073.

(45) Doane, L. M.; Fatiadi, A. J. Electrochemical Oxidation of Croconate Salts; Evidence of the Chemical Equivalence of the Carbonyl Oxygen Atom and the Dicyanomethylene Group. *Angew. Chem. Int. Ed.* **1982**, *21* (8), 635–636. https://doi.org/10.1002/anie.198206351.

(46) Fabre, P.-L.; Dumestre, F.; Soula, B.; Galibert, A.-M. Spectroelectrochemical Behaviour in Dimethylformamide of Pseudo-Oxocarbons Dianions Derived from the Croconate Dianion. *Electrochim. Acta* **2000**, *45* (17), 2697–2705. https://doi.org/10.1016/S0013-4686(00)00324-8.

(47) Doane, L. M.; Fatiadi, A. J. Electrochemical Oxidation of Several Oxocarbon Sals in N,N-Dimethylformamide. *J. Electroanal. Chem.* **1982**, *135*, 193–209.

(48) Armstrong, C. G.; Hogue, R. W.; Toghill, K. E. Application of the Dianion Croconate Violet for Symmetric Organic Non-Aqueous Redox Flow Battery Electrolytes. *J. Power Sources* **2019**, *440*, 227037. https://doi.org/10.1016/j.jpowsour.2019.227037.

(49) Soula, B.; Marie Galibert, A.; Donnadieu, B.; Fabre, P.-L. Diversity of the Coordination Modes of Croconate Violet. Crystal Structures, Spectroscopic Characterization and Redox Studies of Mono-, Di- and Poly-Nuclear Iron(Ii) Complexes. *Dalton Trans.* **2003**, *0* (12), 2449–2456. https://doi.org/10.1039/B300960M.

(50) Soula, B.; Galibert, A.-M.; Donnadieu, B.; Fabre, P.-L. Complexation of Croconate Violet with Copper(II). Crystal Structures, Spectroscopic Characterizations and Redox Studies. *Inorg.Chim. Acta* **2001**, *324* (1), 90–98. https://doi.org/10.1016/S0020-1693(01)00560-6.

(51) Dumestre, F.; Soula, B.; Galibert, A.-M.; Fabre, P.-L.; Bernardinelli, G.; Donnadieu, B.; Castan, P. Synthesis and Characterization of Cobalt(II) Complexes of Croconate and Dicyanomethylene-Substituted Derivatives†. *J. Chem. Soc., Dalton Trans.* **1998**, No. 24, 4131–4138. https://doi.org/10.1039/A807687A.

(52) Castro, L. F.; Almeida, T. C.; Soares Júnior, A. L.; Yoshida, M. I.; Machado, F. C.; Diniz, R.; de Oliveira, L. F. C. Crystal Structures and Raman Spectroscopic Study of Croconate Violet Salts with Alkaline Earth Ions. *Vib. Spectrosc.* **2010**, *54* (2), 112–117. https://doi.org/10.1016/j.vibspec.2010.04.008.

(53) Faria, L. F. O.; Soares Jr, A. L.; Diniz, R.; Yoshida, M. I.; Edwards, H. G. M.; de Oliveira, L. F. C. Mixed Salts Containing Croconate Violet, Lanthanide and Potassium Ions: Crystal Structures and Spectroscopic Characterization of Supramolecular Compounds. *Inorg. Chim. Acta* **2010**, *363*, 49–56.

(54) Chagas, L. H.; Janczak, J.; Machado, F. C.; Oliveira, L. F. C. de; Diniz, R. Dipotassium Tetra-aqua-bis-[3,5-Bis-(Dicyano-methyl-ene)Cyclo-pentane-1,2,4-Trionato(1−)-KN]Cobaltate(II). *Acta Cryst E* **2010**, *66* (12), m1673–m1674. https://doi.org/10.1107/S1600536810048646.

(55) Teles, W. M.; de A. Farani, R.; Speziali, N. L.; Yoshida, M. I.; de Oliveira, L. F. C.; Machado, F. C. K2[Zn(CV)2(H2O)2]·2H2O: The First Zn(II) Complex Structurally Characterized Containing the Pseudo-Oxocarbon Croconate Violet (CV^{2-}). *Inorg. Chim. Acta* **2006**, *359* (10), 3384–3388. https://doi.org/10.1016/j.ica.2006.04.005.

(56) Teles, W. M.; Farani, R. de A.; Maia, D. S.; Speziali, N. L.; Yoshida, M. I.; de Oliveira, L. F. C.; Machado, F. C. Crystal Structure, Thermal Analysis and Spectroscopic Properties of Tetrabutylammonium 3,5-Bis(Dicyanomethylene)-Cyclopentane-1,2,4-Trionate: An Intriguing Pseudo-Oxocarbon and Its Zinc(II) Complex. *J. Mol. Struc.* **2006**, *783* (1), 52–60. https://doi.org/10.1016/j.molstruc.2005.08.020.

(57) Teles, W. M.; Farani, R. de A.; Yoshida, M. I.; Bortoluzzi, A. J.; Hörner, M.; de Oliveira, L. F. C.; Machado, F. C. Synthesis and Crystal Structure of a Novel Zn(II) 2-D Coordination Polymer Containing 1,3-Bis(4-Pyridyl)Propane Ligand and Croconate Violet Dianion. *Polyhedron* **2007**, *26* (7), 1469–1475. https://doi.org/10.1016/j.poly.2006.11.016.

(58) Yang, Q.; Liu, Y.; Ou, H.; Li, X.; Lin, X.; Zeb, A.; Hu, L. Fe-Based Metal–Organic Frameworks as Functional Materials for Battery Applications. *Inorg. Chem. Front.* **2022**, *9* (5), 827–844. https://doi.org/10.1039/D1QI01396C.

(59) Himes, V. L.; Mighell, A. D.; Hubbard, C. R.; Fatiadi, A. J. New Bond-Delocalized Dianions: The Crystal Structure of 1, 3-Bis(Dicyanomethylene) Croconate Salt (C LlN40 3K2 • 2H20). *J. Res. Natl. Inst. Stand.* **1980**, *85* (2), 87–97.

(60) Abreu, H. A. D.; Júnior, A. L. S.; Leitão, A. A.; De Sá, L. R. V.; Ribeiro, M. C. C.; Diniz, R.; de Oliveira, L. F. C. Solid-State Experimental and Theoretical Investigation of the Ammonium Salt of Croconate Violet, a Pseudo-Oxocarbon Ion. *J. Phys. Chem. A* **2009**, *113* (23), 6446–6452. https://doi.org/10.1021/jp901021c.